

## Extended-field electromagnetic model for inductively coupled plasma

This content has been downloaded from IOPscience. Please scroll down to see the full text.

2001 J. Phys. D: Appl. Phys. 34 1897

(<http://iopscience.iop.org/0022-3727/34/12/321>)

View [the table of contents for this issue](#), or go to the [journal homepage](#) for more

Download details:

IP Address: 157.89.65.129

This content was downloaded on 28/11/2014 at 20:49

Please note that [terms and conditions apply](#).

# Extended-field electromagnetic model for inductively coupled plasma

Siwen Xue, Pierre Proulx and Maher I Boulos

Plasma Technology Research Center (CRTP), University of Sherbrooke, Sherbrooke, Quebec, Canada J1K 2R1

Received 18 January 2001

## Abstract

An extended-field (EF), two dimensional (2D) model formulation is proposed for inductively coupled plasma. By extending the calculating domain of the electromagnetic (EM) field outside of the plasma discharge region, the boundary conditions of vector potential used by the standard (ST) 2D model are replaced by simpler far field boundary conditions. The extended model converges faster than the standard formulation and gives rise to consistent solutions throughout the computational domain. Vector potential equations are solved with corresponding continuity, momentum, and energy transfer equations using the commercial code 'FLUENT'. The computational domain for vector potential equations are extended well beyond the induction coil region, while for all the other equations, computations are limited to the discharge region inside the plasma confinement tube. The computational results are compared with those obtained using the ST 2D model. The difference between the results of the two models is noted mostly in the entrance regions of the flow, and close to the induction coil. To validate the EF model, a load with constant electric conductivity is placed centrally in the coil region and the calculated radial profile of the axial magnetic field is compared with existing analytical solutions. The results are in good agreement within an uncertainty of 1%.

## 1. Introduction

By means of ohmic heating, a gas in an inductive coupled plasma (ICP) torch can be heated to a plasma state with maximum temperature in the 10 000–11 000 K range. Over the past three decades numerous applications have been developed for this type of plasma source, especially for material processing such as powder spheroidization, the deposition of protective coatings and of near net shape parts [1]. The plasma synthesis of ultra-fine nanostructure powder [2] is another area where inductive plasma offers important advantages over the alternative technologies. Induction plasmas have also been traditionally used for materials testing in the aerospace industry in order to evaluate the performance of the thermal protection system of re-entry space vehicles [3].

Mathematical modelling is an excellent tool that has so far been used with considerable success to calculate the flow, temperature, and concentration fields in induction plasma over a wide range of operating conditions [4–11]. Significant progress has been made in modelling the induction plasma from one-dimensional electromagnetic (1DEM) models of the early seventies to recent 2DEM models. The milestones in this

field are the models of Boulos [12], Mostaghimi and Boulos [13], Mckelliget *et al* [14] and Proulx and Bilodeau [15].

Though quite accurate and physically correct, the standard 2D ICP models require a lengthy iterative process to converge. The main difficulty arises from the boundary conditions of the vector potentials, which strongly depend on the current density and its distribution in the plasma. The latter depends in turn on the boundary values of the vector potential. This strong nonlinear coupling leads to slow convergence of the solution. For convergence reasons, most (ST) 2DEM models neglect the boundary value of the real part of the vector potential generated by standard current in the plasma. Thus the real part of the vector potential depends mainly on the coil current and the imaginary part is induced in turn from the real part. This makes the solution converge easily, at least for the vector potential equation because there is no strong coupling between plasma current and boundary value of the vector potential. Even so, it is still difficult to obtain the converged solution under certain operating conditions using the ST model. Recently, Vandan and Degrez [16] extended the calculating region to outside of the plasma. The coil is assumed to be a series of parallel current carrying rings that are infinitely thin. In such a case,

the electric field induced by the coil current is singular and so it is split into  $E_v$  and  $E_p$ .  $E_v$  is the singular part induced by the coil current, which has an analytical solution,  $E_p$  is the non-singular part induced by the current in the plasma. The equation for  $E_p$  is solved and,  $E_v$  is taken as a source term of the equation for  $E_p$ . In a real situation, however, the current carrying rings of the coil are not infinitely thin. Moreover, the current elements in the ring may not be all in phase. All of these considerations may influence the solution.

In this paper we extend the calculating domain to the region well outside of the plasma discharge. The current carrying rings in this case are not assumed to be infinitely thin and the diameter of the ring is taken to be 6 mm, which is typical of a coil tube diameter normally used for inductive plasma generation. The singularity of an electric field induced by the coil current is accordingly eliminated. For the finite size ring, the current induced in the coil turn by the current in the plasma and the coil itself are neglected. This means that no current is induced in the coil by an induced electric field.

## 2. Model formulation

### 2.1. The basic assumptions

- The plasma torch is modelled by a fully axisymmetric configuration.
- The coil consists of parallel current carrying rings with a circle cross section, 6 mm in diameter. This implies neglecting the axial component of the coil current.
- Two-dimensional velocity, temperature and EM field.
- Steady state, laminar pure argon plasma flow at atmospheric pressure.
- Optically thin plasma under local thermodynamic equilibrium (LTE) conditions.
- Viscous dissipation and pressure work in the energy equation are neglected.
- Negligible displacement current.

While most of these assumptions are well accepted and have regularly been used in previous modelling studies, special attention should be given to the representation of the induction coil in the model. It is difficult at this stage to evaluate the importance of the assumption of neglecting the induction of current in the coil by the induced electric fields, and that of neglecting the axial currents in the coil. The former will be important only in the calculation of the current distribution in the coil and the apparent coil impedance as seen by the power supply. Neither of these points are covered by the present study and accordingly have no influence on the results of the study. As for neglecting the axial coil current, this could have an influence on the flow and temperature fields in the discharge, especially for a coil with a relatively large pitch. Including the axial coil currents in our calculations will represent a major undertaking and is well beyond the scope of the present study.

### 2.2. Vector potential formulation

The EM field in all the calculating domains is governed by the Maxwell equations which can be written as:

$$\nabla \cdot \mathbf{E} = 0 \quad (1)$$

$$\nabla \cdot \mathbf{H} = 0 \quad (2)$$

$$\nabla \times \mathbf{E} = -\mu_0 \frac{\partial \mathbf{H}}{\partial t} \quad (3)$$

$$\nabla \times \mathbf{H} = \mathbf{J}. \quad (4)$$

Here  $\mathbf{E}$  and  $\mathbf{H}$  are electric and magnetic field intensities, respectively,  $\mu_0$  is the permeability of the free space,  $\sigma$  is the electric conductivity and  $\mathbf{J}$  the total current density. In the above equations it is assumed that no charge is accumulated in the calculating domain and there is no displacement current.

The total current density  $\mathbf{J}$  consists of  $\mathbf{J}_{coil}$ , the current density induced by voltage applied to the two ends of the coil, and  $\mathbf{J}_{ind}$ , the current density developed in the plasma and the coil by the induced electric field.  $\mathbf{J}$  can be written as

$$\mathbf{J} = \mathbf{J}_{coil} + \mathbf{J}_{ind}. \quad (5)$$

From equation (2) the magnetic field intensity can be expressed as

$$\mu_0 \mathbf{H} = \nabla \times \mathbf{A}. \quad (6)$$

Substitution of (6) into (3), and considering that in the absence of an electrostatic field in the plasma the scalar potential equals zero, gives the following equation for electric field intensity

$$\mathbf{E} = -\frac{\partial \mathbf{A}}{\partial t} \quad (7)$$

Taking curl on both sides of equation (4) by using the relation  $\nabla \times \nabla \times \mathbf{A} = \nabla(\nabla \cdot \mathbf{A}) - \nabla^2 \mathbf{A}$  and  $\nabla \cdot \mathbf{A} = 0$ , we get

$$\nabla^2 \mathbf{A} = -\mu_0(\mathbf{J}_{coil} + \mathbf{J}_{ind}). \quad (8)$$

If the current densities in (8) are known, (8) has an analytical solution, which is

$$\mathbf{A} = \frac{\mu_0}{4\pi} \int \frac{\mathbf{J}_{coil}(r, t') + \mathbf{J}_{ind}(r', t')}{|r - r'|} dv' \quad (9)$$

where  $dv'$  is the volume element and the integration is over all the current carrying regions. If coil current density is given, vector potential  $\mathbf{A}$  can be obtained by solving integration equation (9) because the induced current densities in the plasma can be expressed in terms of vector potential  $\mathbf{A}$ .

Assuming sinusoidal coil current variation is with a frequency  $f$ ,  $\mathbf{A}$ ,  $\mathbf{E}$  and  $\mathbf{H}$  will also vary with the same frequency  $f$ . Therefore, the time variation of  $\mathbf{A}$  and  $\mathbf{J}$  in equation (8) can be eliminated [13] and the vector potential equation (8) remains the same but now  $\mathbf{A}$  and  $\mathbf{J}$  will not change with time.

For the standard induction plasma torch, if the coil is assumed to be composed of parallel rings, the electric field, and thus the vector potential, only have the tangential component, i.e.

$$\mathbf{A} = (0, A_\theta, 0). \quad (10)$$

By using (10), equation (8) can be written as follows:

$$\nabla^2 A_\theta - A_\theta/r^2 = -\mu_0(J_{coil} + J_{ind}) \quad (11)$$

where

$$\nabla^2 = \frac{1}{r} \frac{\partial}{\partial r} \left( r \frac{\partial}{\partial r} \right) + \frac{\partial^2}{\partial z^2}$$

Once  $A_\theta$  is obtained, the EM field can be obtained by the following relations:

$$E_\theta = -i\omega A_\theta \quad (12)$$

$$\mu_0 H_z = \frac{1}{r} \frac{\partial}{\partial r} (r A_\theta) \quad (13)$$

$$\mu_0 H_r = -\frac{\partial}{\partial r} A_\theta. \quad (14)$$

As shown in figure 1 the calculating domain is divided into five zones. Zone I represents the plasma flow, zone II the coil, zone III the plasma confinement quartz tube, zone IV the quartz tube to separate central and sheath gas and zone V the region of ( $R_0 + \delta_W < r < R_{el}$ ) except the coil zone. The grids are shown on the right side of the figure. In the following we present the forms of equation (11) in the different zones.

In plasma,  $J_{ind} = \sigma E = -i\omega\sigma A_\theta$  and  $J_{coil} = 0$  so that

$$\nabla^2 A_\theta - (1/r^2 + i\omega\mu_0\sigma) A_\theta = 0 \quad (15)$$

or

$$\nabla^2 A_{\theta R} - (1/r^2) A_{\theta R} + \omega\mu_0\sigma A_{\theta I} = 0$$

$$\nabla^2 A_{\theta I} - (1/r^2) A_{\theta I} - \omega\mu_0\sigma A_{\theta R} = 0$$

where  $A_{\theta R}$  and  $A_{\theta I}$  are the real and the imaginary parts of the vector potential, respectively.

In the coil:

$$\nabla^2 A_\theta - A_\theta/r^2 = -\mu_0 J_{coil} \quad (16)$$

or

$$\nabla^2 A_{\theta R} - A_{\theta R}/r^2 = -\mu_0 J_{coil}$$

$$\nabla^2 A_{\theta I} - A_{\theta I}/r^2 = 0.$$

Here we have assumed that the electric conductivity of the coil is zero, which means  $J_{ind}$  in the coil is zero.  $J_{coil} = I_l/(\pi a^2)$  is uniformly distributed over the cross section of the coil conductor. For the given 6 mm diameter of the coil conductor, the current density distributions across the conductor have no influence on the plasma flow. Our computational results also indicate that the shape of the cross section of the current carrying conductor (circles, squares or a long rectangle to represent a few rings) has no influence on plasma flow. From this we may deduce that there would be no influence on plasma flow even if coil conductors were hollow, which is the case when using water-cooled tubes for induction coil design.

In the other zones (zones III, IV and V), there is no current source so that:

$$\nabla^2 A_\theta - A_\theta/r^2 = 0. \quad (17)$$

Here we have assumed that the electric conductivity of quartz tubes is zero. The real and imaginary parts of the vector potentials have the same form.

### 2.3. Boundary conditions of vector potentials

For the outer boundary conditions, because of the distance from the current carrying coil, we can set:

$$A_{\theta R} = 0 \quad \text{and} \quad A_{\theta I} = 0. \quad (18)$$

The boundary conditions (18) are equivalent to the boundary conditions on the metal surfaces with electric conductivity

being infinite. To check whether the outer boundary is far enough from the coil we use different positions of the outer boundary for the calculation. The farther the boundary position is from the coil the better, but it takes more computer time because of the increase in the number of grid nodes. The acceptable distance for the positioning of the outer boundary is determined empirically through the successive solution of the same equations with different position of the boundary. The outer boundary is finally set at a level at which the results of two successive solutions are essentially identical, indicating that the outer boundary does not need to be moved any further.

For the boundary conditions at the interfaces between different zones we assume continuity of the vector potentials cross the interfaces without jumping. This implies that the magnitude and the direction of  $A_{\theta R}$  and  $A_{\theta I}$  remain unchanged on both sides of the interfaces. Physically this is not necessarily consistent since a change in the dielectric properties of the material across the interface would result in a corresponding difference in the normal component of the electric field, and hence of the vector potential. It is difficult, however, in the FLUENT code to set different boundary conditions on the two sides of an interface. For the interfaces shown in figure 1 the electric field and, accordingly, the vector potential are parallel to the interfaces so that the continuity in the boundary conditions can be applied.

### 2.4. Governing equations

Continuity:

$$\frac{\partial(\rho u)}{\partial z} + \frac{1}{r} \frac{\partial(\rho r v)}{\partial r} = 0. \quad (19)$$

Momentum:

$$\begin{aligned} \rho u \frac{\partial u}{\partial z} + \rho v \frac{\partial u}{\partial r} = & -\frac{\partial p}{\partial z} + 2 \frac{\partial}{\partial z} \left( \mu \frac{\partial u}{\partial z} \right) \\ & + \frac{1}{r} \frac{\partial}{\partial r} \left[ \mu r \left( \frac{\partial u}{\partial r} + \frac{\partial v}{\partial z} \right) \right] + F_z + F_{z\_brake} \end{aligned} \quad (20)$$

$$\begin{aligned} \rho u \frac{\partial v}{\partial z} + \rho v \frac{\partial v}{\partial r} = & -\frac{\partial p}{\partial r} + \frac{\partial}{\partial z} \left[ \mu \left( \frac{\partial v}{\partial z} + \frac{\partial u}{\partial r} \right) \right] \\ & + \frac{2}{r} \frac{\partial}{\partial r} \left[ \mu r \frac{\partial v}{\partial r} \right] + F_r + F_{r\_brake}. \end{aligned} \quad (21)$$

Energy:

$$\begin{aligned} \rho u \frac{\partial h}{\partial z} + \rho v \frac{\partial h}{\partial r} = & \frac{\partial}{\partial z} \left( \frac{\lambda}{C_p} \frac{\partial h}{\partial z} \right) + \frac{1}{r} \frac{\partial}{\partial r} \left[ r \frac{\lambda}{C_p} \frac{\partial u}{\partial r} \right] \\ & + P - R - P_{loss}. \end{aligned} \quad (22)$$

Here  $u$  and  $v$  are the axial and radial velocity components, respectively,  $\rho$ ,  $\mu$ ,  $\lambda$ , and  $C_p$  are the density, viscosity, thermal conductivity, and specific heat at constant pressure, respectively,  $h$  is the enthalpy,  $p$  is the pressure, and  $P$  and  $R$  are the ohmic heating power and the volumetric radiation heat loss, respectively.

The Lorentz forces and heating power are expressed as:

$$F_r = \frac{1}{2} \mu_0 \sigma \text{Re} (E_\theta H_z^*) \quad (23)$$

$$F_z = -\frac{1}{2} \mu_0 \sigma \text{Re} (E_\theta H_r^*) \quad (24)$$

$$P = \frac{1}{2} \sigma \text{Re} (E_\theta H_z^*). \quad (25)$$

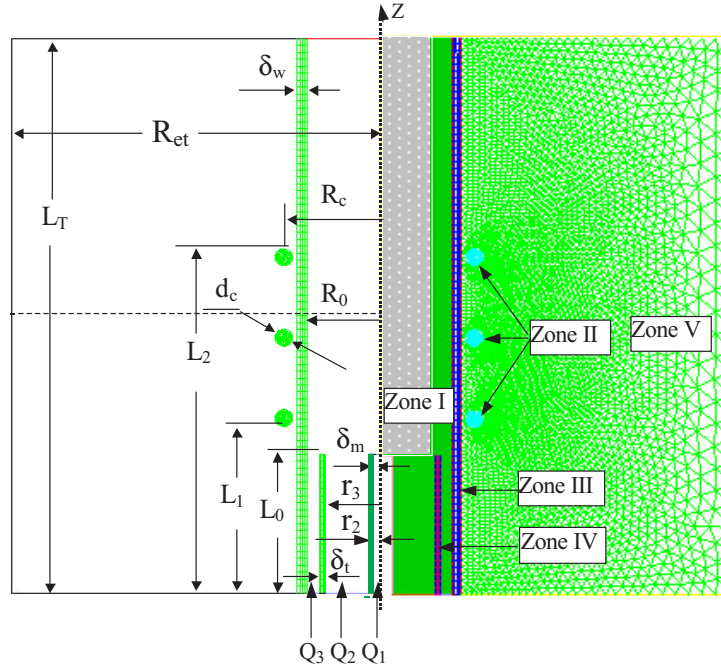


**Figure 1.** Torch geometry. The ST model solves the governing equations only in the region of  $L_0 < z < L_T$  and  $0 < r < R_0$ . The load of constant electrical conductivity is placed in the light grey region with white dots. The parameters are defined on the left-hand side and the computational grid and zones are shown on the right-hand side. All the radial profiles are drawn at the horizontal dashed line ( $z = 102$  mm).

The superscript \* denotes the conjugate. Other than the plasma zone,  $F_r$ ,  $F_z$  and  $P$  are all equal to zero. For the FLUENT code, all governing equations need to be solved in all the zones identified in figure 1. Other than the plasma zone we use a source term ( $F_{z\_brake}$  or  $F_{r\_brake}$ ) for each of the momentum equations to counteract the inertia forces and achieve a no flow situation. Outside the plasma confinement tube a source term ( $P_{loss}$ ) is added to the energy equation to keep the temperature constant in that region.

$$F_{r\_brake} = -10^{20}v \quad (26)$$

$$F_{u\_brake} = -10^{20}u \quad (27)$$

$$P_{loss} = -10^{30}(T - T_0). \quad (28)$$

The other boundary conditions used for the solution of the governing equations are similar to those described in [13].

### 3. Results and discussion

In this section, computational results from the extended-field (EF) model are presented and compared in detail with the ST model developed by Proulx and Bilodeau [15]. Both the EF and ST models were solved for the same torch geometry (Tekna model PL-50) with a 50 mm id plasma confinement tube. Details of the principal dimensions of the torch, identified in figure 1, are given in table 1. The calculation domain for the EF model was extended to outside of the plasma region, while for the ST model it was limited to the plasma zone, defined by  $L_0 < z < L_T$  and  $r < R_0$ . A summary of the operation parameters used for the computations are also listed in table 1. The working gas (sheath, central and carrier gas) was argon. The governing equations and vector potential equations were solved by FLUENT with  $54 \times 80$  quadrilateral cells in

the plasma region and quartz tubes, and a total of 7489 non-structural triangular cells in the coil and the outside region, as shown on the right side of figure 1. The radius of the outer boundary was taken to be 12.5 cm, which is five times the radius of the plasma confinement tube. Computation carried out with a radius of 150 mm for the external boundary did not reveal any difference in the results in the discharge region. Subsequent computations were carried out in this case with a radius of 125 mm for the location of the external boundary. In order to calibrate the model a limited number of calculations were carried out for a cylindrical metallic load with constant electrical conductivity. The load used in this case was 37.6 mm in diameter and 150 mm long, centrally placed inside the coil, as shown on the right side (light grey region with white dots) of figure 1. Then the calculated profile of the axial magnetic field was compared with the skin depth obtained from EM theory. When the electrical conductivity of the load was zero (vacuum), the analytical result for the intensity of the axial magnetic field at the axis was compared with the computational result.

#### 3.1. Magnetic field distribution for constant electric conductivity load

To get the radial distribution of the axial magnetic field in the presence of constant electric conductivity load, only vector potential equations were solved by FLUENT. Computations were carried out for five cases, one of which corresponded to operating the torch without a load (electrical conductivity of zero for vacuum). The other four cases were calculated for a load with electrical conductivities of 100, 500, 1500 and  $2500 \Omega^{-1} \text{ m}^{-1}$ . These correspond to the conditions for an argon plasma at temperatures less than 10 000 K. The coil current was set to be 161 A, which corresponds to the current

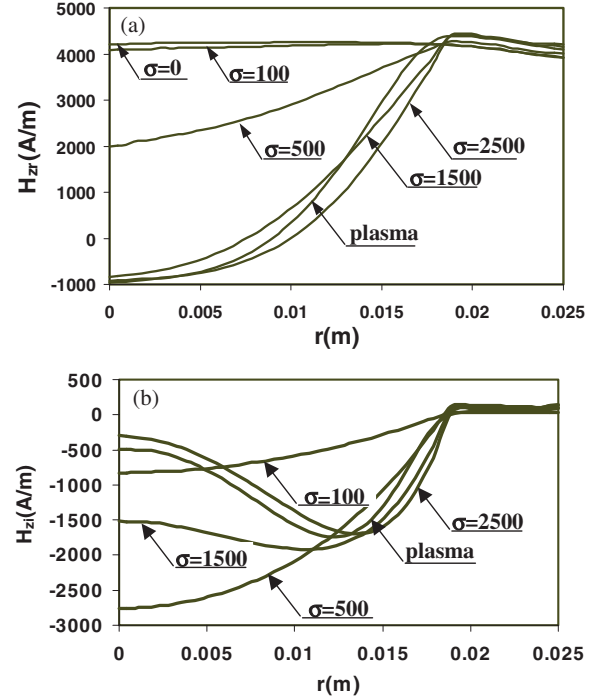
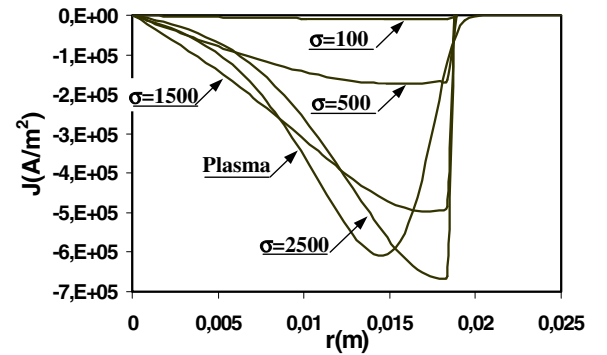
**Table 1.** Torch characteristic dimensions and operation conditions.

$\delta_m = 2.0$ mm	$L_0 = 50$ mm	$R_0 = 25$ mm	$Q_1 = 1.0$ slpm	$P_{ohmic} = 5$ kW
$r_2 = 3.7$ mm	$L_1 = 60$ mm	$R_c = 33$ mm	$Q_2 = 3.0$ slpm	$f = 3$ MHz
$r_3 = 18.8$ mm	$L_2 = 124$ mm	$d_c = 6$ mm	$Q_3 = 31.0$ slpm	
$R_{et} = 125$ mm	$L_T = 200$ mm	$\delta_t = 2.2$ mm	$\delta_w = 3.5$ mm	

needed to dissipate 5 kW in an argon plasma with a sheath gas flow rate of 31 slpm (standard litre per minute). The calculated radial profiles of the axial magnetic field at  $z = 102$  mm are shown in figures 2(a) and (b) for the real and imaginary parts, respectively. In the case of the vacuum, only the real part of the magnetic field is shown in figure 2(a). There is no curve in figure 2(b) because there is no induced current in the load. As expected, the results show a uniform distribution of the magnetic field, in this case across the radius of the plasma torch. With the increasing electrical conductivity of the load (100, 500, 1500 and 2500  $\Omega^{-1} \text{ m}^{-1}$ ) the magnetic field intensity in the centre of the coil drops rapidly. The radial magnetic field profile for the case of argon plasma is superimposed on the figure for comparison. As noted, the curve for the plasma is similar to the curves for  $\sigma = 1500$  and 2500  $\Omega^{-1} \text{ m}^{-1}$ . The curve for  $\sigma = 2500 \Omega^{-1} \text{ m}^{-1}$  begins to drop once the magnetic field enters the load at  $r = 18.8$  mm, while the curve for plasma decreases at about  $r = 17.5$  mm. The form of the profiles reflects the combined effects of the magnetic field generated by the real part of the induced current distributions in the plasma, shown in figure 3, with the applied magnetic field generated by the coil current in the absence of the load ( $\sigma = 0$ ). From figure 3, the peak current density for the constant electric conductivity load is at the outer edge of the load,  $r = 18.8$  mm, while that for plasma case is at  $r = 14.3$  mm. In the region of  $r > 21$  mm, the plasma current density is almost zero since the electrical conductivity of the gas in this region is almost zero. For an oscillator frequency of 3 MHz, the skin depths, as calculated from  $\delta = (2/\mu_0\sigma\omega)^{1/2}$ , are 29, 13, 7.5, 5.8 mm when  $\sigma$  equals 100, 500, 1500, 2500  $\Omega^{-1} \text{ m}^{-1}$ , respectively. The profiles of the magnetic field, shown in figure 2(a) and the induced current density distributions (figure 3) are consistent with the values of skin depths.

It may be noted that when the electrical conductivity is higher than 1500  $\Omega^{-1} \text{ m}^{-1}$  and in the case of plasma, the axial magnetic field near the axis of the coil is negative compared to the axial magnetic field outside of the load or in the outer region of the plasma discharge zone. These results may be reasonable because the current induced in the plasma is in the opposite direction with respect to the coil current and the magnetic field near the axis, generated by the current in the plasma or the load, may be higher than that generated by the coil current. In the cases of plasma and higher electrical conductivity load the intensities of the axial magnetic fields in the external non-conducting region of flow ( $18.8 < r < 25$  mm) are slightly stronger. That is because the magnetic fields generated in this region by both coil current and load or plasma current are in the same direction. In the case of vacuum ( $\sigma = 0$ ), as shown in figure 2(a),  $H_z$  at the axis and  $z = 102$  mm is 4210 A m $^{-1}$ . The analytical result of  $H_z$  at the same point can be derived as

$$H_z = \sum_{i=1}^3 \frac{I_i r_c^2}{2 r_i^3} = 4258 \text{ (A m}^{-1}\text{)}. \quad (29)$$

**Figure 2.** Radial profiles at  $z = 102$  mm of the axial magnetic field  $H_z$  for different electrical conductivities of the load (a) real parts; (b) imaginary parts.**Figure 3.** Radial profiles at  $z = 102$  mm, of the real part of the induced current density for different electrical conductivities of the load.

Here we assume that the three-turn coil is infinitely thin and the summation is over all the current carrying rings.  $r_i$  is the distance from the point in the ring to the field point and  $r_c$  is the radius of the ring. The 1% error may come from the assumption that the ring is infinitely thin. Comparisons prove that our model is quite accurate to within less than 1%. Figure 2(b) shows the profiles of the imaginary part of the axial magnetic field which are generated by the imaginary part of the current in the plasma or load. Figure 4 shows the corresponding isocontour of the real part (a) and the imaginary part (b) of



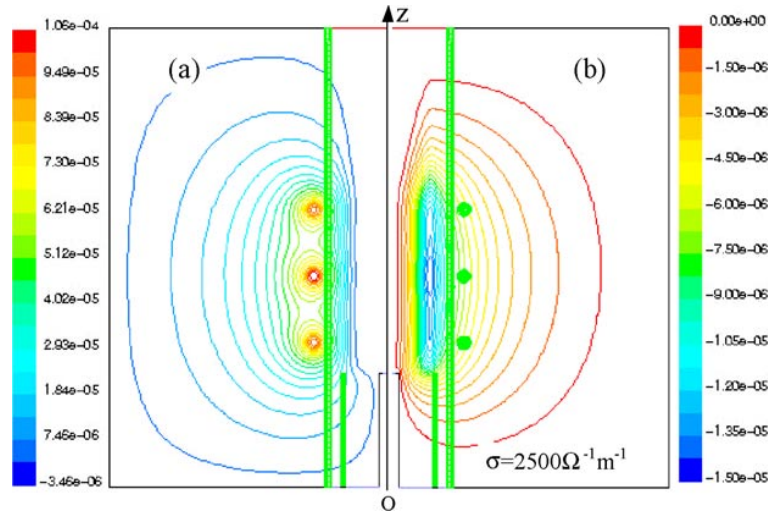


**Figure 4.** Isocontour of the vector potentials for a load with an electric conductivity of  $2500 \text{ } (\Omega^{-1} \text{ m}^{-1})$ : (a) real part ( $A_{\theta R}$  (T m): maximum =  $1.01 \times 10^{-4}$ , minimum =  $1.51 \times 10^{-6}$ , incremental value =  $4.985 \times 10^{-6}$ ); (b) imaginary part. ( $A_{\theta i}$  (T m): maximum =  $-6.844 \times 10^{-7}$ , minimum =  $-1.369 \times 10^{-5}$ , incremental value =  $6.5 \times 10^{-7}$ ).

the vector potentials for a constant electric conductivity of  $\sigma = 2500 \text{ } \Omega^{-1} \text{ m}^{-1}$ .

### 3.2. Comparison between ST model and EF model

In the following, computations were repeated for the same plasma case with the ST and EF models. The operating conditions are summarized in table 1. Figures 5 and 6 show the real and imaginary parts of the vector potentials, respectively. On each of these two figures part (a) shows the results for the EF model while part (b) shows the corresponding field obtained from the ST model. The ST model solves governing equations only in the plasma discharge region while the EF model solves governing equations over all the extended regions well beyond the plasma discharge region. The gas inlet boundary for the ST model is placed at the position of  $z = 50 \text{ mm}$ . Because it is too close to the current sources, the gas inlet boundary for the EF model is extended 50 mm upstream of that location to the position of  $z = 0$ . The other difference is that the ST model neglects the boundary value for the real part of the vector potential equations produced by the current in the plasma, which may not be justifiable because the current in the plasma is comparable to the coil current. This leads to an important difference in the coil current needed to sustain the 5 kW argon plasma discharge. The coil current needed is 161 A, according to the EF model, compared with 109 A for the ST model. As shown in figures 5 and 6, the EF model provides a more realistic distribution of the vector potential field in comparison to the ST model, which obviously severely truncates the field along the boundaries of the calculation domain. The effect is particularly significant on the upstream boundary at  $z = 50$ , and along the wall of the plasma confinement tube. The reason for this is that the boundary condition for the ST model is not appropriate since it is too close to the coil. The real part of the vector potentials in the region of  $60 < z < 124 \text{ mm}$  and  $15 < r < 25 \text{ mm}$  predicted by the EF model changes along the  $z$  direction while the real part of the vector potentials from the ST model in the same region is almost uniform along the  $z$  direction. The imaginary

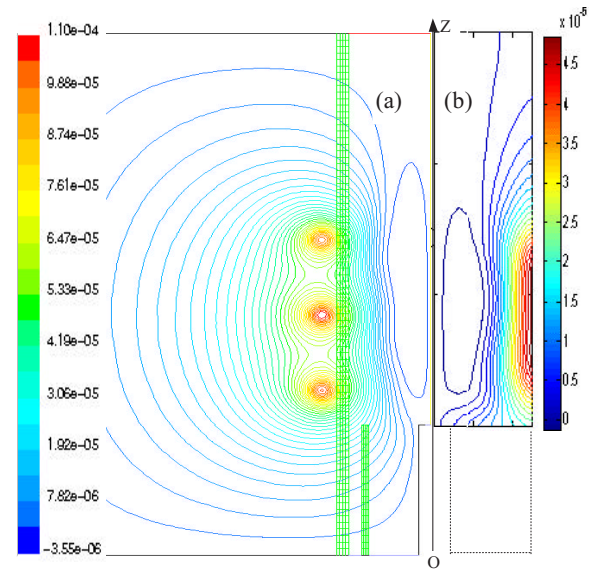


**Figure 5.** Isocontour of the real part of the vector potential for an argon plasma: (a) EF model ( $A_{\theta R}$  (T m): maximum =  $1.07 \times 10^{-4}$ , minimum =  $-5.87 \times 10^{-7}$ , incremental value =  $3.0 \times 10^{-6}$ ); (b) ST model. ( $A_{\theta R}$  (T m): maximum =  $4.74 \times 10^{-5}$ , minimum =  $-6 \times 10^{-7}$ , incremental value =  $3.0 \times 10^{-6}$  and operating conditions are given in table 1).

part of the vector potential in the plasma from the EF model shows two peaks which are due to the relatively large pitch of the induction coil used (pitch = 32 mm, three-turn coil of total length 64 mm). The pitch to coil diameter ratio in this case is 0.5. As shown in figure 6(b), the effect is not depicted by the ST model, which reveals only a single peak in the vector potential distribution along the wall of the plasma confinement tube. Comparing figures 5(a) and 6(a) with figure 4 it is noted that the vector potential for the case of a plasma load is similar to that for a load with constant electrical conductivity.

The profiles for an axial magnetic field along the centreline of the plasma discharge computed using the EF and ST models

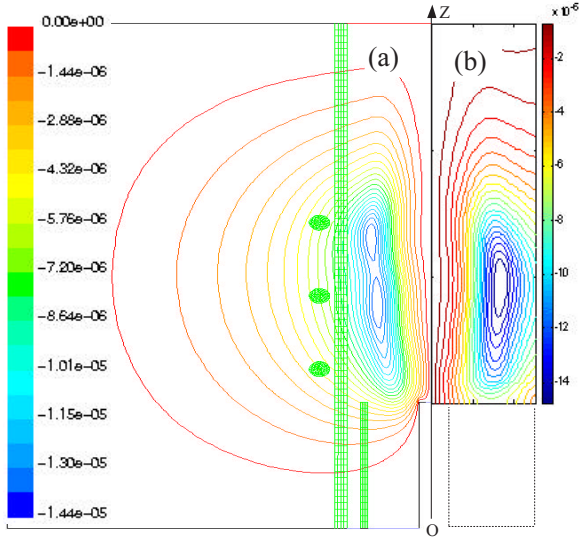


**Figure 6.** Isocontour of the imaginary part of the vector potential for an argon plasma: (a) EF model; (b) ST model. ( $A_{\theta I}$  (T m): maximum =  $-7.2 \times 10^{-7}$ , minimum =  $-1.37 \times 10^{-5}$ , incremental value =  $7.22 \times 10^{-7}$  and operating conditions are given in table 1).

are shown in figure 7. Significant differences are noted in figure 7(a) between the profiles for the real part of the vector potentials predicted by the EF and ST models in the upstream region of flow ( $z < 120$  mm). The difference between the predictions of the two models in the imaginary part, as shown in figure 7(b), is of the order of 10–20%. The corresponding radial profiles of the axial magnetic field at  $z = 102$  mm are shown in figure 8. The largest difference between the predictions of the two models is noted in the real part of the axial magnetic field in figure 8(a) in the outer discharge region at  $r > 18$  mm. This results from the fact that the ST model neglects the boundary values for the real part of the vector potential, generated by the induced current in the plasma. The difference between the imaginary parts of the vector potentials the EF calculated with the ST models results from the real parts because they are coupled to each other. The corresponding radial profiles for the local electrical field distribution in the plasma at  $z = 102$  mm, are shown in figure 9. The difference in the tangential electric field  $E_{\theta}$  values between the predictions of the EF and ST model, is again mostly in the outer region of the plasma discharge. The biggest difference is about 15%. From figures 5–9 we can see that the EF model gives a better representation of the EM field as it uses more realistic boundary conditions. Because of the observed differences in the EM fields predicted by the EF and ST models, the local power dissipation and radial Lorentz forces in the plasma vary between the two models, as shown in figures 10 and 11, respectively. The power dissipation and radial Lorentz forces from the EF model show a double peak, reflecting the coil pitch in this case. The maximum radial Lorentz force predicted by the ST model is almost 20% higher than that predicted by the EF model. A similar difference of the order of 22% is also noted in the maximum power dissipation in the plasma predicted by the ST model compared to the EF model.

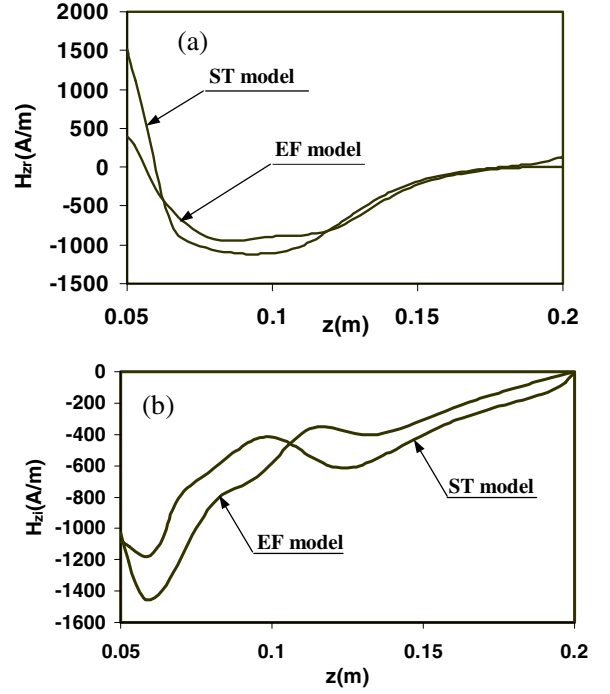


**Figure 7.** Axial profiles of the axial magnetic field along the centreline for argon plasma: (a) real parts; (b) imaginary parts (operating conditions are given in table 1).

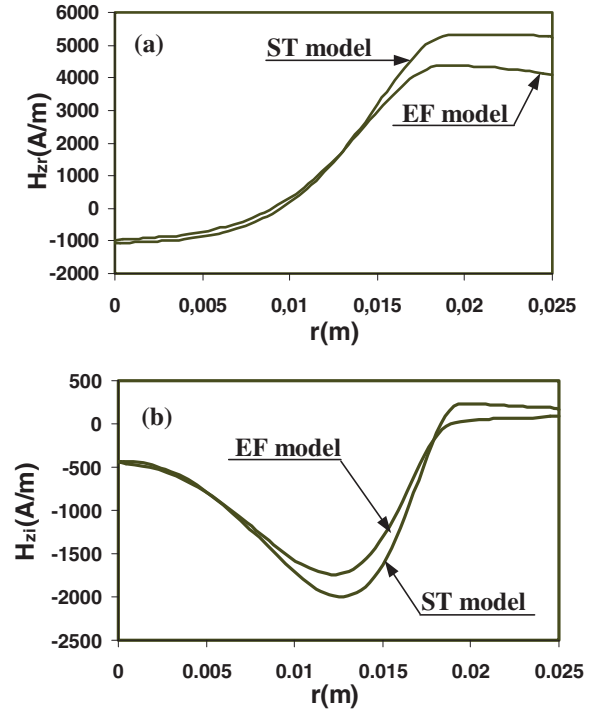


**Figure 8.** Radial profiles of the axial magnetic field for argon plasma: (a) real parts; (b) imaginary parts (operating condition are given in table 1).

### 3.3. Effects on flow and temperature field

Due to the observed difference in the EM fields predicted by the EF and ST models, it is not surprising to observe differences in the corresponding temperatures and flow fields, as shown



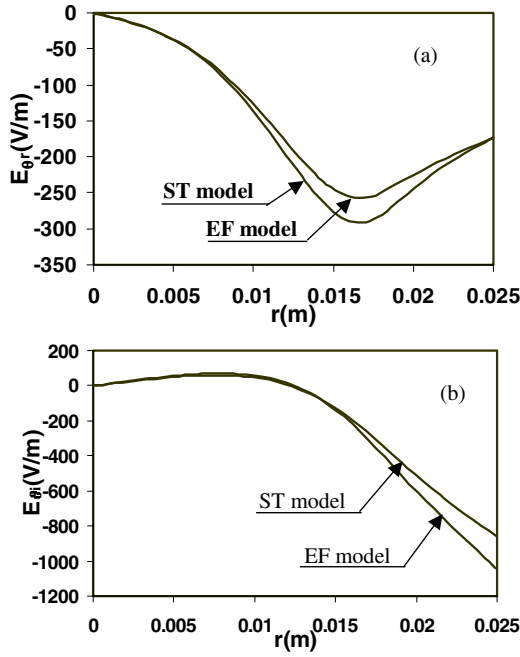


**Figure 9.** Radial profiles of the tangential electric field  $E_\theta$ , at  $z = 102$  mm, for argon plasma: (a) real parts; (b) imaginary parts (operating conditions are given in table 1).

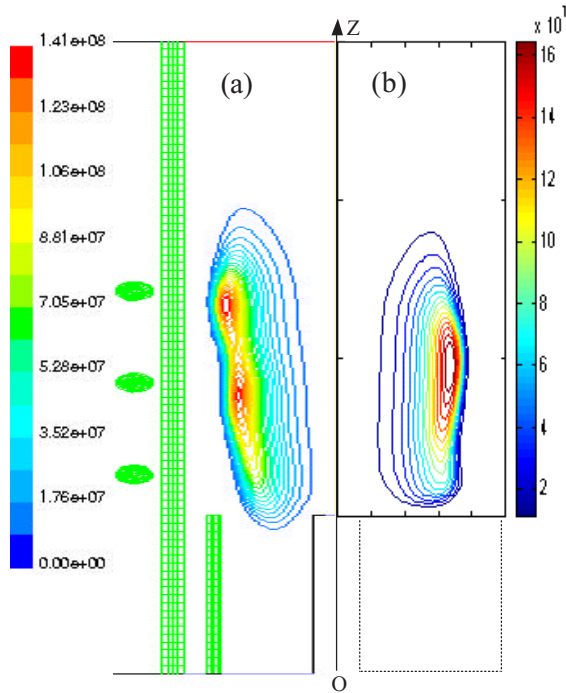


**Figure 10.** Isocontour of the power dissipation in the plasma for argon plasma. (a) EF model; (b) ST model ( $P_d$  ( $\text{J m}^{-3}$ ): maximum =  $1.366 \times 10^8$ , minimum =  $6.507 \times 10^6$ , incremental value =  $6.5 \times 10^6$  and operating conditions are given in table 1).

in figures 12 and 13, respectively. The difference between the temperature fields predicted by the two models is quite significant at  $z = 50$  mm. In the region  $z < 50$  mm, the temperature from the EF model is significantly higher than 300 K, normally set by the ST model. The difference can be attributed to reverse flow of the plasma that brings

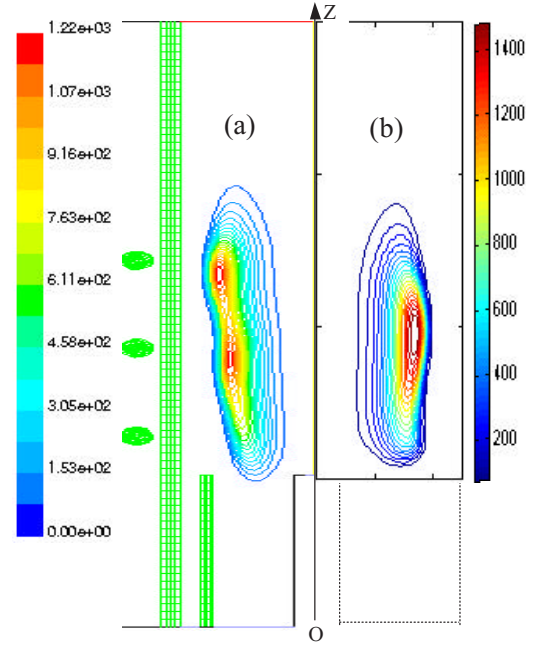


**Figure 11.** Isocontour of the radial Lorentz force for argon plasma. (a) EF model; (b) ST model. ( $-F_r$  ( $\text{N m}^{-3}$ ): maximum = 1169.55, minimum = 55.7, incremental value = 55.7 and operating conditions are given in table 1).

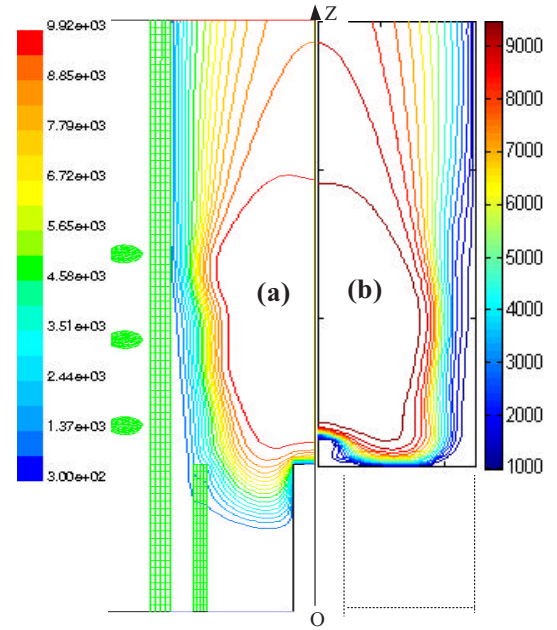


**Figure 12.** Temperature isocontour for argon plasma: (a) EF model; (b) ST model. ( $T$  (K): maximum = 9440.2, minimum = 781, incremental value = 481 and operating conditions are given in table 1).

high-temperature gas into the upstream region at  $z < 50$  mm. In the central discharge region, however, the temperature fields predicted by both models are in general agreement, though the shapes of the isocontour are not completely identical. The observed differences in stream functions between the EF and ST models can be attributed to the difference in the distributions of radial Lorentz force in plasma.

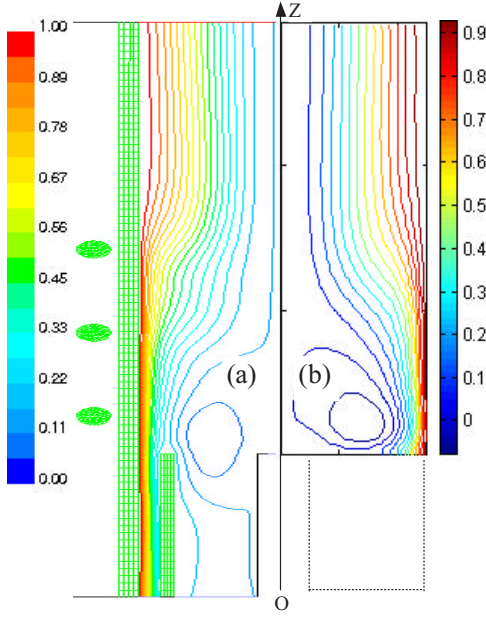


**Figure 13.** Stream function isocontour for argon plasma: (a) EF model; (b) ST model (contour is normalized to one and operating conditions are given in table 1).

The temperature and velocity distributions along the centreline are shown in figure 14. Significant differences are observed in the temperature profiles in the entrance region of the discharge at  $z < 50$  mm. Beyond that point,  $z > 59$  mm, the temperatures along centreline of the plasma discharge predicted by both models are identical. A significant difference is observed, however, in the velocity profiles predicted by the two models. As shown in figure 14(b), the difference is not limited, however, to the entrance region, but is also noted in the centre and the downstream end of the discharge.

The axial profiles of integrated power dissipation resulting from the EF and ST models are shown in figure 15. These are computed using the following equation:

$$P(z)/P_0 = (1/P_0) \int_0^a P(r, z) 2\pi r dr \quad (30)$$

where  $a$  is the radius of the plasma column and  $P_0$  is the total ohmic power (5 kW). It is noted from figure 15 that the EF model gives rise to a significantly different power distribution in the discharge region compared to that of the ST model. The difference is mostly noted at the downstream end of the coil.

#### 4. Conclusion

In our present study, a 2D EF, electromagnetic model formulation is used for the computation of flow and temperature fields in an inductively coupled discharge using the FLUENT code. The principal contribution of the present investigation is in the adaptation of the new EM field definition to a standard commercial CFD code, and the demonstration that considerable care should be applied to the definition of the computation domain. While the increase in the computation domain is associated with a corresponding increase in the computation time, an optimal boundary position needed to

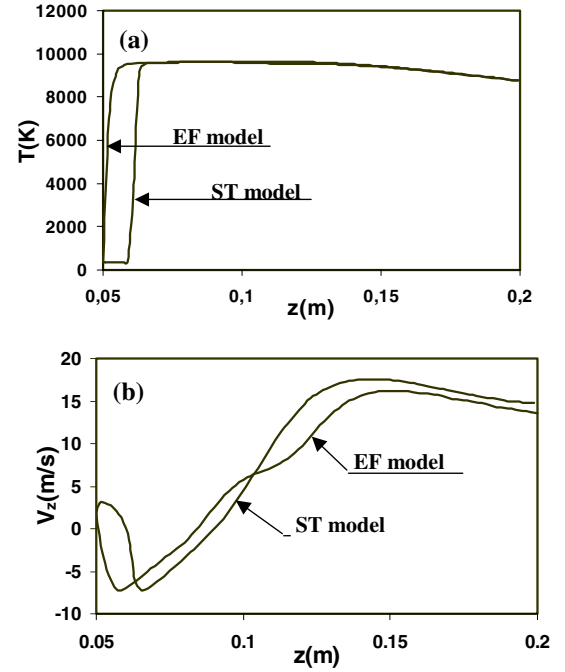


**Figure 14.** Axial profiles of temperature and axial velocity along the centreline for argon plasma (a) temperature; (b) axial velocity (operating conditions are given in table 1).

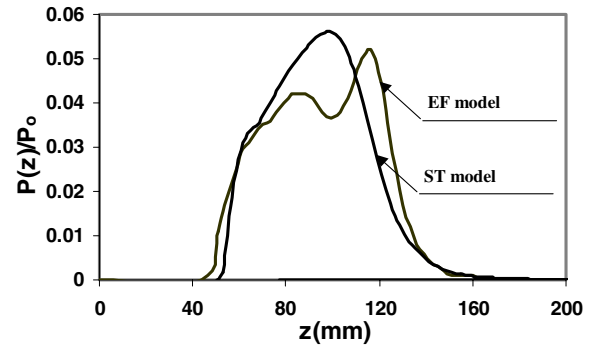


**Figure 15.** Axial integrated power dissipation profiles (operating conditions are given in table 1).

be identified, on a case by case basis, not to compromise the quality of the results.

To validate the EF model, computations were carried out for a load with constant electrical conductivity placed into the centre of the coil region. The computed radial distribution of the axial magnetic field was compared with the values of skin depth predicted using the simple channel model ( $\delta = 2/(\mu_0 \sigma \omega)^{1/2}$ ). These were in good agreement with model predictions. When the electrical conductivity of the load was zero (vacuum) the calculated axial magnetic field was also in good agreement with the analytical result.

For an inductive plasma under typical operation, the EM, flow and temperature fields obtained from the EF model were only slightly different from those obtained using the ST model. The significance of the present model is, however, its ability to predict the effects of coil geometry on the EM, flow and temperature fields. It provides a more realistic representation of the EM field in the neighbourhood of the coil region.

## Acknowledgment

The financial support of the Natural Sciences and Engineering Research Council of Canada (NSERC) and the Ministry of Education of the province of Québec through its (FCAR) program are gratefully acknowledged.

## References

- [1] Boulos M I M I 1997 *High Temp. Mater. Proc.* **1** 17–39
- [2] Gitzhofer F 1996 *Pure Appl. Chem.* **68** 1113
- [3] Bottin B, Carbonaro M, Paris S, Vander Haegen V, Nevelli V and Venneman D 1988 *Proc. 3rd European Workshop on TPS (ESTEC, Noordwijk)*
- [4] Boulos M J 1985 *Pure Appl. Chem.* **57** 1321
- [5] Miller R C and Ayen R J 1969 *J. Appl. Chem.* **40** 5260
- [6] Chen X and Pfender E 1991 *Plasma Chem. Plasma Proc.* **11** 103
- [7] Yang P and Barnes R M 1989 *Spectrochim. Acta B* **44** 657
- [8] Proulx P, Mostaghimi J and Boulos M I M I 1991 *Int. J. Heat Mass Transfer* **34** 2571
- [9] Mostaghimi J, Proulx P and Boulos M I M I 1985 *J. Numer. Heat. Transfer* **8** 187
- [10] Colombo V, Panciatici C, Zazo A, Cocito G, and Cognolato L 1997 *IEEE Trans. Plasma Sci.* **25** 1073
- [11] Bernardi D, Colombo V, Coppa G G M, and D'Angola A *Euro. Phys D* at press
- [12] Boulos M I 1976 *IEEE Trans. Plasma Sci.* **4** 28
- [13] Mostaghimi J and Boulos M I 1989 *Plasma Chem. Plasma Proc.* **9** 25
- [14] Mckelliget J 1986 *Technical Report* 86-112.1, College of Engineering, University of Lowell, MA
- [15] Proulx P and Bilodeau J-F 1991 *Plasma Chem. Plasma Proc.* **11** 371
- [16] Vandan A D and Degrez G 1998 *Technical Paper* 98-2825, AIAA, Albuquerque, NM